



Research Paper

Chromium (VI) removal kinetics by magnetite-coated sand: Small-scale flow-through column experiments

Julian Sorwat^a, Adrian Mellage^b, Markus Maisch^a, Andreas Kappler^a, Olaf A. Cirpka^b, James M. Byrne^{c,*}^a Geomicrobiology, Center for Applied Geoscience, University of Tübingen, Schnarrenbergstr 94-96, 72076 Tübingen, Germany^b Hydrogeology, Center for Applied Geoscience, University of Tübingen, Schnarrenbergstr 94-96, 72076 Tübingen, Germany^c School of Earth Sciences, Wills Memorial Building, University of Bristol, Bristol BS8 1RJ, United Kingdom

ARTICLE INFO

Editor: Dr. Xiaohong Guan

Keywords:

Cr(VI)
Remediation
Chemisorption
Reactive-transport model

ABSTRACT

Magnetite nanoparticles are promising materials for treating toxic Cr(VI), but safe handling is challenging due to their small size. We prepared flow-through columns containing 10% or 100% (v/v) magnetite-coated sand. Cr(VI) removal efficiency was determined for different Cr(VI) concentrations (0.1 or 1.0 mM), neutral or alkaline pH, and oxic/anoxic conditions. We formulated a reactive-transport model that accurately predicted total Cr removal, accounting for reversible and irreversible (chemi)sorption reactions. Our results show that the material removes and irreversibly sequesters Cr(VI). For the concentration range used 10% and 100% (v/v) -packed columns removed > 99% and 72% of influent Cr(VI), respectively. Two distinct parameter sets were necessary to fit the identical model formulation to the 10 or 100% (v/v) columns (e.g., maximum sorption capacities (q_{\max}) of 1.37 $\mu\text{mol Cr/g}$ sand and 2.48 $\mu\text{mol Cr/g}$, respectively), which we attributed to abrasion-driven magnetite micro-particle detachment during packing yielding an increase in reactive surface area. Furthermore, experiments under oxic conditions showed that, even when handled in the presence of O_2 , the magnetite-coated sand maintained a high removal capacity (47%). Our coupled experimental and modelling analyses indicates that magnetite-coated sand is a promising and suitable medium for treating Cr(VI)-contaminated water in fixed-bed reactors or permeable reactive barriers.

1. Introduction

Providing access to clean drinking water is a fundamentally important, but also greatly challenging problem facing mankind (Brezonik and Arnold, 2012). One particular contaminant which continues to gain interest is chromium (Cr), with an increasing number of studies reporting trace levels of Cr(VI) in drinking water (US Environmental Protection Agency, 1987; World Health Organization, 1996; Harijan and Chandra, 2016; Meranger et al., 1979) and an expanding number of articles focusing on Cr toxicity (Jin et al., 2016; Kaprara et al., 2015). Chromium use is widespread in different industries such as leather tanning, metallurgy, electroplating, alloying or textile dyes, and can be released via effluents to aquatic ecosystems (Avudainayagam et al., 2003; Owlad et al., 2009; Sharma et al., 2008). Additionally, natural sources can result in elevated Cr(VI) concentrations in waters which come into contact with ultramafic rocks (Fantoni et al., 2002; Robles-Camacho and Armienta, 2000; Saputro et al., 2014). In its

reduced state, Cr(III) can readily be oxidized to Cr(VI) by Mn in field soils (Bartlett and James, 1979) or manganese oxides in aquatic environments (Richard and Bourg, 1991). The safe limits for total chromium in drinking water are set to 50 $\mu\text{g/L}$ in Europe (European Commission, 1998) or 100 $\mu\text{g/L}$ in the US (US Environmental Protection Agency, 2009). However, these values do not distinguish between Cr oxidation states. Conversely, regulations in California, for example, consider oxidation states for which the set Maximum Contaminant Level (MCL) for Cr(VI) to 10 $\mu\text{g/L}$ (Kaprara et al., 2015), highlighting the higher toxicity of Cr(VI).

In the environment, the two most stable oxidation states of chromium are trivalent Cr(III) and hexavalent Cr(VI). Cr(III) is an essential trace nutrient which helps maintaining an effective lipid, protein, and glucose metabolism. Cr(VI), by contrast, is toxic and carcinogenic, and can diffuse through cell membranes and oxidize biological molecules (Barnhart, 1997). In the environment, Cr(VI) is highly mobile due to its speciation as weakly sorbing chromate CrO_4^{2-} or dichromate $\text{Cr}_2\text{O}_7^{2-}$. Cr

* Corresponding author.

E-mail address: james.byrne@bristol.ac.uk (J.M. Byrne).<https://doi.org/10.1016/j.jhazmat.2021.125648>

Received 17 December 2020; Received in revised form 25 February 2021; Accepted 10 March 2021

Available online 18 March 2021

0304-3894/© 2021 Elsevier B.V. All rights reserved.

(III) in contrast, mainly forms poorly soluble oxyhydroxides at neutral pH and sorbs to mineral surfaces (e.g., clay minerals, iron or manganese oxides) (Richard and Bourg, 1991).

Iron(II)-containing minerals have been shown to be an effective reductant for several contaminants including Cr(VI) (Fendorf et al., 2000). Promising results have been achieved using magnetite (Fe_3O_4), a magnetic, mixed-valent iron oxide, as adsorbent material for the removal of Cr(VI) from the aquatic environment (Crean et al., 2012; Cutting et al., 2010; Sorwat et al., 2020). Unlike other iron minerals, Cr(VI) not only electrostatically adsorbs onto charged magnetite surfaces, but it also reacts with structural Fe(II) and is reduced to Cr(III) which is then incorporated into the octahedral sites of the magnetite structure (Cutting et al., 2010; Fendorf and Li, 1996; Jung et al., 2007).

A large proportion of literature investigating the use of magnetite to treat Cr has so far focused on nanoparticles (Crean et al., 2012; Ren et al., 2017; Sundman et al., 2020) due to their large surface-to-volume ratio which is then associated with an enhanced adsorption and reduction potential for Cr(VI) compared to adsorbents with a larger particle size. While nanoparticles show a high adsorption potential, it is challenging to use them in practice (Zach-Maor et al., 2011). Due to their small particle size, it is difficult and expensive to separate them from the aqueous solution, e.g., by using external magnetic fields or centrifugation and filtration (Kango and Kumar, 2016), which is necessary when applying the nanoparticles in ex-situ water treatment. In porous media, such as fixed-bed reactors or in in-situ remediation schemes, they may coagulate and cause clogging (Kango and Kumar, 2016; Chahbani and Tondeur, 2001; Verbinen et al., 2013; Phenrat et al., 2010). Once released to the aquatic environment, the high specific area can further decrease due to agglomeration with other (nano)particles and therefore lead to a loss of contaminant removal capacity (Petosa et al., 2010; Phenrat et al., 2009; Tratnyek and Johnson, 2006). Therefore, immobilization of magnetite onto a Supporting material can be used to overcome some of these problems in flow-through systems whilst maintaining an enhanced contaminant removal capacity similar to that of free nanoparticles (Sorwat et al., 2020; Zach-Maor et al., 2011). In a report released in 2004, the Royal Society and Royal Academy of Engineering stated (Royal and Royal, 2004): “We recommend that the use of free (that is, not fixed in the matrix) manufactured nanoparticles and environmental applications such as remediation be prohibited until appropriate research has been undertaken and it can be demonstrated that the potential benefits outweigh the potential risks.”

There are yet further challenges when considering the use of magnetite under real-world conditions. For example, chromite ore processing residues (COPR) are a substantial source of Cr pollution in the environment. Usually, these residues are very alkaline, with pH values between 11 and 12 (Geelhoed et al., 2002). Additionally, in oxic systems, Fe(II) in magnetite can be oxidized which reduces the ability of magnetite to reduce and remove Cr(VI) (Eary and Rai, 1988; Pettine et al., 1998).

In a previous study, we performed batch experiments to determine the removal capacity of magnetite-coated sand grains towards Cr(VI) and compared the efficiency of the coating to that of magnetite nanoparticles (Sorwat et al., 2020). Therein, we showed that, via a sand coating procedure, magnetite can be fixed in place and maintain nanoparticle-like reactivity towards Cr(VI) removal. Nevertheless, batch studies cannot directly be applied to scaled-up systems such as permeable reactive barriers because the solid-to-water ratio is much higher in porous media than in suspensions, the access to reactive sites may be hindered in porous media, and the intricate interplay between solute transport, sorption, and redox reactions lead to concentration fronts moving through the system (Bailey et al., 1992). Thus, to assess the irreversibility of removal processes in flow-through systems, such as fixed-bed reactors and permeable reactive barriers, well-controlled experiments mimicking such systems are paramount (Sperlich et al., 2005).

In this study, we combined scanning electron microscope (SEM)

imaging, energy-dispersive X-ray (EDX) analysis, breakthrough curve (BTC) monitoring and solid-bound Fe or Cr extractions to quantify the Cr-removal capacity of magnetite coated quartz sand in flow-through systems. Water-saturated columns (10 mL glass syringes), packed with either magnetite coated sand or with clean quartz sand and a thin layer of magnetite in the mid-section of the columns, were subjected to pulse injections of Cr(VI) under various conditions, including a range of Cr(VI) concentrations, neutral and high pH, as well as oxic and anoxic conditions to determine their influence on Cr(VI) removal efficiency. By fitting a reactive-transport model to both solid- and aqueous-phase measurements we aim to quantify the contribution of reversible and irreversible (chemi-)sorption of Cr onto magnetite and assess the potential use of magnetite coated sand as a Cr(VI) removal agent.

2. Material and methods

2.1. Magnetite coated sand synthesis

Abiogenic magnetite coated quartz sand (grain size range 0.4–0.8 mm) was synthesized via the addition of a FeCl_2 (1 M)/ FeCl_3 (2 M) in HCl (0.3 M) solution to 300 g batches of acid washed (1 M HCl) sand. The mixture was stirred manually during the drop-wise addition of NH_4OH (20%) in an anoxic glovebox (MBraun, 100% N_2). The magnetite coated sand coating procedure and the corresponding physical and chemical properties of the material are described in detail in our previous study (Sorwat et al., 2020). Additionally, the related porosity and dispersion coefficient are given in the [Supplementary information](#) (Fluorescein tracer experiment).

2.2. Column setup

Experiments were conducted in a series of small-scale flow-through columns using 10 mL glass syringes (wall thickness: 1 mm, length: 83 mm, inner diameter: 15 mm, FORTUNA® OPTIMA®, Poulten & Graf). The columns (i.e., glass syringes) were dry-packed in a glovebox (100% N_2) with sand using one of two configurations. Either the total column volume was packed with magnetite coated sand, or the columns were packed in a layered configuration, where a thin layer of magnetite (10% of the volume) was packed in between two layers of clean sand. The two setups will be referred to herein as 100% and 10% magnetite coated sand, respectively. After packing, the columns were sealed with a butyl rubber stopper. A schematic of the column setup is shown in [Figs. S1 and S2](#).

At the top and the bottom of the column a filter paper (pore size 12–25 μm , GE Healthcare Whatman™) was placed to avoid blockage of the outflow channel. After packing, the columns were connected to an inlet reservoir (either Cr(VI), NaHCO_3 , fluorescein solution or tap water) via Tygon tubing (inner diameter: 1 mm, SEAL Analytical, Inc.) connected to a multi-channel peristaltic pump (IPC 12 channel, ISMA-TEC®). Bicarbonate buffer (NaHCO_3) was added to maintain a constant pH throughout the experiment. All Tygon tubing was flushed with N_2/CO_2 (v/v; 90/10) for 10 min before the columns were connected to ensure no oxygen was left in the tubes. Columns were connected to a valve which was in turn connected to a needle inserted into the sampling bottles. The valve was closed during the exchange of sampling vials to avoid a loss of liquid sample and was opened again after sampling. A syringe filled with N_2/CO_2 (v/v; 90/10) was connected to the inlet reservoir to ensure a constant pressure during the experiment. Additionally, an empty syringe was connected to the sampling bottle for overpressure compensation. The columns were equipped with O_2 -sensitive optode sensor foil to regularly monitor the oxygen concentration using a FiBox (FiBox 3, PreSens, Regensburg, Germany) during the experimental run using the internal software (OxyView-PST3-V5.32).

2.3. Chromium sorption experiment

Prior to any Cr injections, we performed fluorescein tracer experiments to quantify conservative-transport parameters in the columns, namely the porosity and dispersion coefficient. Details of the tracer breakthrough behaviour are described in the results (see also Fig. S3). Chromium sorption experiments were performed for each column setup (10% or 100% magnetite coated sand) in triplicates. Each column was connected to a reservoir containing pure NaHCO₃ (22 mM) to ensure the pore volume of the column was fully saturated. Once fully saturated, the inlet solution was switched to a reservoir containing K₂CrO₄ (Cr(VI)) in NaHCO₃ (22 mM). All experiments were run for 22 h to capture the complete breakthrough of 3 h pulse injections of Cr. Outflow samples were collected every 15 min for analysis of total Cr and total Fe. Following the 3 h pulse, the inlet solution was exchanged to a Cr-free solution containing pure NaHCO₃ (22 mM) for the remainder of the experiments. The average pumping rate in our experiments was set to 5.1 ± 0.07 mL/h (corresponding to a seepage velocity, *v*, of 1.74 ± 0.017 m/d).

Pulse injections of Cr were conducted with a series of experimental configurations (Table 1): i-iv) Columns were filled with either 10% or 100% magnetite coated sand, and the inlet solution contained Cr(VI) at either 0.1 or 1 mM concentration buffered at pH 7. v) Cr(VI) at 0.1 mM was injected into the 10% magnetite coated sand columns under oxic conditions. vi) the pH of the inlet solution was adjusted to pH 12 with 10 M NaOH and Cr was injected into a 10% magnetite coated packed sand column under anoxic conditions.

2.4. Aqueous-phase analysis

The pH of the solution was frequently measured during the experimental run using pH strips (pH-Box, Merck KGaA).

2.4.1. Total iron and chromium

The samples collected during the sorption experiment and in the inlet reservoir were diluted 1:5 and acidified with 2% HNO₃. The total Cr and Fe concentration in solution in the acidified samples were determined using a microwave plasma-atomic emission spectrometer (Agilent 4200 MP-AES, Agilent Technologies, equipped with the Agilent SPS 3 autosampler) and processed with the internal Agilent MP Expert software (Version 1.5.0.6545). Cr and Fe measurements were performed at a wavelength of 425.433 nm and 371.993 nm, respectively.

2.5. Solid-phase characterization

2.5.1. Total iron, iron(II) and total Cr

After each experimental run, the columns were brought into an anoxic glovebox (MBraun; 100% N₂) to sample the solid phase. For this, each column was separated into 10% slices in separate plastic plates and stored in an anoxic glovebox. To determine the change in oxidation state of iron over the experimental run and extract the iron-associated total Cr, the magnetite coating was dissolved either in 0.5 M HCl over 1 h for the readily extractable iron or in 6 M HCl overnight to measure the change of the bulk material. Extractions were carried out at room temperature in an anoxic glovebox (MBraun; 100% N₂) in triplicates. The

Table 1

Series of experimental configurations performed with a pulse injection of a Cr (VI) solution. Cr(VI) concentrations and pH refer to the inlet solution.

Condition	Magnetite [% v/v]	Cr (VI) [mM]	Oxic/anoxic	pH
i	10	0.1	Anoxic	7
ii	10	1.0	Anoxic	7
iii	100	0.1	Anoxic	7
iv	100	1.0	Anoxic	7
v	10	0.1	Oxic	7
vi	10	0.1	Anoxic	12

total iron (Fe(tot)) and the ferrous iron (Fe(II)) concentrations of the magnetite coated sand were measured for the starting material and after the experimental run applying the spectrophotometric ferrozine assay (Stookey, 1970). Spectrophotometric measurements were performed using the monochromator-based UV/VIS spectrophotometer Multiskan GO (Thermo Fisher Scientific) and processed with the SkanIt software 3.2. Each HCl extraction sample was additionally diluted 1:5 and acidified with 2% HNO₃ for total Cr analysis using a microwave plasma-atomic emission spectrometer (Agilent 4200 MP-AES, Agilent Technologies, equipped with the Agilent SPS 3 autosampler) and processed with the internal Agilent MP Expert software (Version 1.5.0.6545). Cr measurements were performed at a wavelength of 425.433 nm.

2.5.2. Microscopy data

To observe possible changes on the adsorbent surface after the reaction of Cr with magnetite and to gain insight on the elemental composition on the surface of the adsorbent, SEM/EDX was performed using a Crossbeam 550 L dual beam SEM (Zeiss, Oberkochen, Germany) equipped with field emission gun and ULTIM MAX (Oxford instruments, Halifax Rd, UK) EDX detector. Magnetite coated sand grains were collected before and after the experimental run. The samples were dried at 30 °C in an anoxic glovebox after each sorption experiment and then fixed to carbon tape pads (1 cm²) placed on an aluminium SEM sample holder. The samples were sputter coated with 8 nm platinum by a SALTEC SCD 500 with a working distance of 35 mm over 90 s at 0.02 mbar. SEM micrographs were collected at several magnifications using the Secondary Electrons Secondary Ions (SESI) detector. For the EDX analysis, data were collected with 30 kV acceleration voltage, 5 mm working distance and 39x magnification. To obtain comparable results, each sample was measured with identical parameters using a scan time of 20 min

2.5.3. Reactive-transport model

We simulated one-dimensional advective-dispersive transport of Cr (VI) coupled to sorption onto magnetite and reduction of adsorbed Cr (VI) to Cr(III) by starting with the mass balance of combined Cr(VI) and Cr(III):

$$\frac{\partial C}{\partial t} + \frac{(1-\phi)\rho_s}{\phi} \frac{\partial S}{\partial t} + v \frac{\partial C}{\partial x} - D \frac{\partial^2 C}{\partial x^2} = 0 \quad (1)$$

in which *C* [μmol/L] and *S* [μmol/g] are the aqueous- and solid-phase concentrations of total Cr, respectively, *φ* [-] is the porosity of the sand pack, *ρ_s* [kg/L] is the mass density of the solids (here, the mass density of the quartz sand, 2.65 [kg/L]), *v* [m/s] is the linear velocity, *D* [m²/s] denotes the dispersion coefficient, whereas *t* and *x* are the temporal and spatial coordinates. Eq. (1) is subject to a known-flux boundary condition at the inlet, and a zero-dispersive flux boundary condition at the outlet.

Sorption of Cr(VI) was simulated as a combination of reversible and irreversible (chemisorption) processes. Reversible sorption was formulated via a linear-driving-force approximation, driven by the difference between equilibrium and actual concentrations of sorbed Cr(VI), *S*_{Cr(VI)}^{EQ} and *S*_{Cr(VI)} [μmol/g] (analogous to the approach by Mikutta et al. (2009)):

$$S_{Cr(VI)}^{EQ} = q_{max} \frac{C_{Cr(VI)}}{K_{ads} + C_{Cr(VI)}} \quad (2)$$

$$r_{sorb} = k_{sorb} (S_{Cr(VI)}^{EQ} - S_{Cr(VI)}) \quad (3)$$

in which *C*_{Cr(VI)} [μmol/L] is the aqueous-phase concentration of Cr(VI), and equilibrium is described by Langmuir sorption, with *q_{max}* [μmol Cr/g sand] being the maximum sorption capacity, *K_{ads}* [μmol L⁻¹] the binding constant, and *k_{sorb}* [s⁻¹] the kinetic sorption rate constant.

Reduction of bound Cr(VI) to Cr(III), parameterized in Eq. (4), reduces the sorption capacity q_{max} . Sorption of Cr(VI) onto clean quartz sand was considered by assigning a maximum sorption capacity to the quartz sand, constituting a fraction of that of magnetite by multiplying q_{max} by a dimensionless factor, f_{sand} .

In addition to reversible sorption, Cr(VI) can undergo chemisorption. The chemisorption reaction involves the reduction of Cr(VI) coupled to the oxidation of magnetite-associated Fe(II). The reduced Cr(III) product is incorporated into the magnetite structure. We assumed that Cr(VI) must be adsorbed first to the magnetite, before being reduced, and that the reduction was irreversible under the experimental conditions. Our conceptual assumptions agree with the proposed “adsorption-reduction” mechanism proposed by Chang et al. (2021). The process of reducing adsorbed Cr(VI) to immobile Cr(III) was parameterized by a second-order rate law:

$$r_{chem} = k_{chem} \cdot S_{Cr(VI)} \cdot S_{Fe(II)} \quad (4)$$

in which k_{chem} [g/μmol/s] is the second-order rate coefficient for the reduction of sorbed Cr(VI) ($S_{Cr(VI)}$) to immobile Cr(III) and $S_{Fe(II)}$ [μmol/g] is the solid phase Fe(II) concentration. The latter facilitated the inclusion of an oxygen dependence of Cr sorption on the magnetite coated sand. Under oxic conditions, Fe(II) can be oxidized to Fe(III), thereby reducing the rate of chemisorption. The oxidation of ferrous iron by oxygen was also parameterized as a second-order rate:

$$r_{ferrox} = k_{ferrox} \cdot C_{O_2} \cdot S_{Fe(II)} \quad (5)$$

in which k_{ferrox} [L/μmol/s] is the second-order rate coefficient for the reduction of ferrous iron and C_{O_2} [μM] is the aqueous concentration of oxygen in the pore water.

The final system of governing equations is given by:

$$\frac{\partial C_{Cr(VI)}}{\partial t} = D \frac{\partial^2 C_{Cr(VI)}}{\partial x^2} - v \frac{\partial C_{Cr(VI)}}{\partial x} - \frac{(1-\phi)\rho_s}{\phi} r_{sorb} \quad (6)$$

$$\frac{\partial S_{Cr(VI)}}{\partial t} = r_{sorb} - r_{chem} \quad (7)$$

$$\frac{\partial S_{Cr(III)}}{\partial t} = r_{chem} \quad (8)$$

$$\frac{\partial S_{Fe(II)}}{\partial t} = f_{st} \cdot r_{chem} - 4r_{ferrox} \quad (9)$$

$$\frac{\partial q_{max}}{\partial t} = -f_q \cdot r_{chem} \quad (10)$$

The reduction of adsorbed Cr(VI) by Fe(II) oxidation decreases the maximum sorption capacity, and the rate of chemisorption is multiplied by f_{st} , based on the stoichiometry of reduction reaction, thus the reduction of 1 mol of Cr(VI) yields the loss of f_{st} moles of Fe(II). The stoichiometry of both the chemisorption reaction (r_{chem}) and the subsequent reduction in sorption capacity associated with the oxidation of Fe(II) and the loss of Fe(II)-binding sites, f_{st} and f_{q} , respectively, were set as fitting parameters. We justify our choice due to an observed deviation from the expected Cr(VI):Fe(II) stoichiometry of 1:3 in all of our experiments, where Cr(VI) reduction led to an almost three-fold higher than expected Fe(II) loss. The latter is in agreement with previous findings where Cr(VI) reduction led to a higher Fe(II) loss than explained by Fe(III) production alone (Crean et al., 2012; Cutting et al., 2010; Telling et al., 2009). The choice of two separate parameters, f_{st} and f_{q} , is justified by the fact that not all sorption binding sites are Fe(II) sites, and that Fe(III) sites can also contribute to reversible Cr(VI) sorption (Singh et al., 1993).

Spatial discretization was done by the finite volume method, converting the transport and reaction Eqs. 6–10 to a nonlinear system of ordinary differential equations which were solved in MATLAB using the ordinary-differential-equation solver `ode15s` (Shampine, 1997). The

model was fitted to the experimental data using the trust-region-reflective method of the MATLAB function `lsqnonlin` (Coleman and Li, 1996), minimizing the sum of squared error between measured data and model output. (Note: it was found that each experiment type required a different set of parameters. This is likely related to the detachment of magnetite nanoparticles during the high-density packing.) To improve the fitting scheme, the cumulative distribution function (CDF) of the breakthrough concentrations was fitted rather than the concentrations themselves.

3. Results and discussion

3.1. Chromium sorption experiment

Fig. 1 shows the measured and simulated breakthrough curves for the different experiments, while Table 2 lists the calculated percentage removal under the different experimental conditions. Therein, the removal of Cr in each column was calculated based on (1) the breakthrough curve (difference between influent and effluent total Cr mass), (2) the solid-phase extracted Cr concentration (see section: Adsorbent characterization), and (3) the results of the reactive-transport model. The BTCs in Fig. 1 are shown over a time-span of 6 h, which corresponded to the complete breakthrough of the Cr pulse over all experiments. Curves for the entire 22-hour experiment are presented in Fig. S4.

For the majority of experimental variants, except for that at pH 12 and the anoxic run with 1 mM Cr in the 10% columns, Cr concentration breakthrough curves were considerably delayed, and exhibited a lower maximum concentration when compared to the conservative (tracer) behaviour. In addition, no Cr was detected at the outflow when 0.1 mM of Cr were injected into a 100% column. This delay is indicative of a reaction of the injected Cr onto the adsorbent material. A long tailing of the Cr breakthrough at concentrations above the limit of quantification, in the effluent during the desorption phase (the re-injection of Cr free solution) would indicate the strong influence of reversible sorption. The absence of such a long tailing for any of our measured BTCs, points to the irreversible nature of Cr chemisorption onto the magnetite coated sand. Thus, the kinetics of the chemisorption are sufficiently fast, in relation to the velocity time scale, to allow for a significant fraction of the injected Cr to be irreversibly assimilated into the magnetite structure via chemisorption. This is an essential point for the application of the magnetite coated sand as a remediation agent, because here we can state that the magnetite coated sand not only removes Cr(VI) from solution, but that once removed, the Cr remains adsorbed even after 19 h (roughly 13.3 pore volumes) of continuous flow-through of a Cr-free solution.

Using the 100% filled column as an example, we can compare the relative speed of both the reversible sorption and chemisorption reaction by multiplying the second-order chemisorption rate constant, k_{chem} , by the initial amount of solid-phase Fe(II). Doing so, yields a pseudo first-order maximum rate constant for chemisorption, which hints at similar kinetics for both steps in the reaction sequence ($k_{chem} \cdot S_{Fe(II)}^{t=0} = 3.84 \times 10^{-5}$ and $k_{sorb} = 4.12 \times 10^{-5} \text{ s}^{-1}$). Furthermore, the fitted parameter values for k_{sorb} and k_{chem} (see Table 3) agree well with previously published estimates of first-order and second-order rate coefficients for the immobilization and reduction of Cr(VI) by solid phase Fe(II) (Xu and Zhao, 2007; Buerge and Hug, 1999). Chang et al. (2021) reported one order of magnitude slower kinetics for the second-order rate of Cr(VI) reduction at magnetite surfaces. We speculate that this discrepancy is driven, in part, by the fact that Chang et al. (2021) performed batch experiments, with a small solid-to-liquid ratio. Higher solid-to-liquid ratios, such as those in sand-packed flow through column experiments have been shown to yield more accurate estimates of reactive parameters, as they better emulate the pore configuration and reactive surface area in natural settings (Wang et al., 2009).

In general, the simulated BTCs almost perfectly reproduce the measured BTCs. Only in the 100% column with, a 1 mM Cr injection at

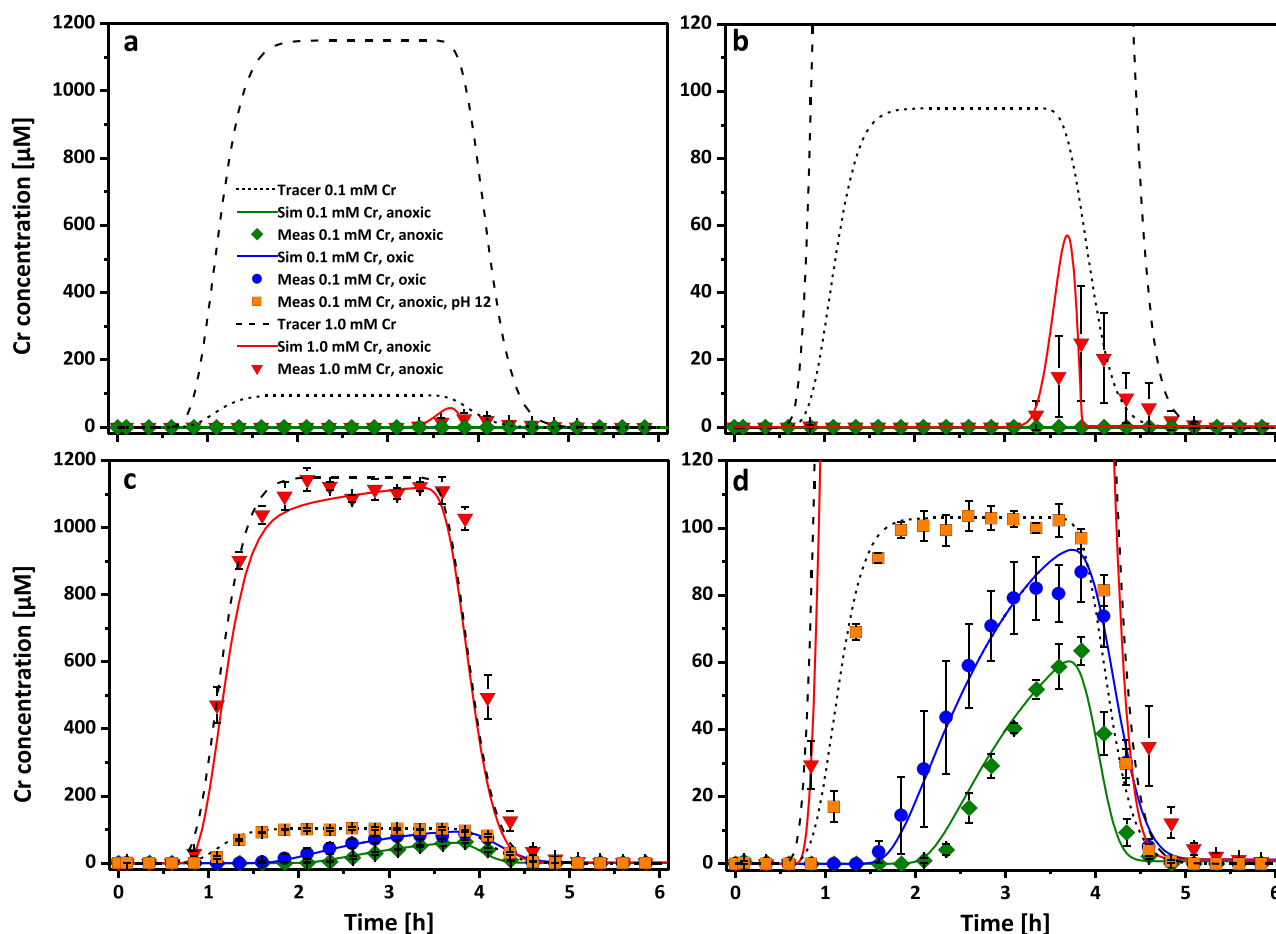


Fig. 1. Cr(VI) breakthrough concentration measurements for a 3 h pulse injection for a+b) 100% magnetite coated sand columns, c+d) 10% magnetite coated sand columns using different column setup parameter. Blue circles: 0.1 mM Cr(VI) injection at pH 7 under oxic conditions; Green diamonds: 0.1 mM Cr(VI) injection at pH 7 under anoxic conditions; Orange squares: 0.1 mM Cr(VI) injection at pH 12 under anoxic conditions; Red triangles: 1 mM Cr(VI) injection at pH 7 under anoxic conditions. The solid lines with the respective colors represent the simulated breakthrough curves. Black dashed and dotted lines represent the simulated breakthrough curve for a 0.1 mM or 1.0 mM tracer, respectively. b and d are the zoomed-in version of a and c in the region of 0–120 μM Cr. (For interpretation of the references to colour in this figure legend, the reader is referred to the web version of this article.)

Table 2

Calculated chromium removal for the column experiments under different conditions. The percentage removal was calculated based on the results of the MP-AES measurements for the sequential or total layer extraction, the calculated amount of Cr passed through the column during the experimental run time and the reactive-transport model. Errors were calculated using the standard deviation of triplicate samples.

Magnetite layer amount	Sequential extraction	Breakthrough	Model
+ adsorbate conditions	Cr removal [%]	Cr removal [%]	Cr removal [%]
10%, 0.1 mM Cr anoxic	57.7 ± 4.7	72.5 ± 1.1	70.1
10%, 0.1 mM Cr oxic	38.1 ± 9.0	47.2 ± 3.1	41.4
10%, 0.1 mM Cr anoxic pH 12	0.0 ± 0.0	3.1 ± 1.1	–
100%, 0.1 mM Cr anoxic	109.9 ± 13.1	100.0 ± 0.0	100.0
10%, 1.0 mM Cr anoxic	5.5 ± 1.2	5.7 ± 0.9	6.6
100%, 1.0 mM Cr anoxic	81.3 ± 12.1	99.4 ± 0.2	99.4

pH 7, does the model predict a sharper BTC, with a higher maximum concentration and an abrupt drop. The measurements, however, suggest that the breakthrough was broader and the concentration drop more gradual. We attribute this discrepancy to dislodgment of micro and nanoparticles of magnetite, which was more pronounced during the packing procedure for the 100% column, as discussed below in reference

to the fitted parameters. We speculate that this effect yields a non-uniform distribution of higher surface area particles that may have accumulated in the outflow filter. Because we are not able to correctly constrain this phenomenon, we decided not to parameterize it in our model, and accept the discrepancy as an unintended consequence of the packing procedure. Despite the slight difference between simulated and measured BTCs, total Cr removal as well as solid-phase concentration profiles agree well also for the 1 mM 100% column and help to provide confidence in the validity of our simulation.

The 100% columns shown in Fig. 1a and b indicate the complete removal of the injected Cr(VI) at an inflow concentration of 0.1 mM Cr in agreement with the model output. Similar efficiencies of 99.4% and 99.4% Cr removal were observed for the measured and modelled BTCs, respectively, at increased Cr concentrations (1.0 mM). For the 10% columns at pH 7 under anoxic conditions, we calculated a removal percentage of 72.5% and 5.7% for 0.1 mM or 1.0 mM Cr(VI), respectively. These results are also in good agreement with the removal percentages calculated by the model (70.1% and 6.6%).

Due to the larger number of binding sites, Cr breakthrough in the 100% columns was only detectable when high concentrations (1 mM) were injected at the inlet. Thus, to better quantify the sorption kinetics of Cr onto the magnetite coated sands and assess the effects of high pH and oxic conditions, we performed additional experiments on the 10% columns only. Additional experimental variants, using the 10% magnetite coated sand filled columns and a 0.1 mM Cr(VI) inflow

Table 3

Calibrated parameter values for both the 10% and 100% magnetite coated sand flow-through experiments.

Parameter	Units	10%	Relative Error	Uncertainty range
q_{max}	[$\mu\text{mol Cr/g sand}$]	1.37	2.16	0.63 to 2.96
	[$\mu\text{mol Cr/g Fe}$]	350.43	2.16	162.33 to 756.50
f_{sand}	[-]	0.011	1.52	0.007 to 0.017
K_{ads}	[$\mu\text{mol/L}$]	1.31	2.64	0.50 to 3.45
k_{sorb}	[1/s]	6.42×10^{-5}	1.71	3.74×10^{-5} to 1.10×10^{-4}
k_{chem}	[g/ $\mu\text{mol/s}$]	5.89×10^{-5}	16.83	3.50×10^{-6} to 9.92×10^{-4}
f_{st}	[-]	10.09	1.47	7.17 to 14.20
f_q	[-]	3.26	2.13	1.53 to 6.96
k_{ferrox}	[L/ $\mu\text{mol/s}$]	5.23×10^{-9}		
		100%	Relative Error	Uncertainty range
q_{max}	[$\mu\text{mol Cr/g sand}$]	2.48	1.05	2.36 to 2.60
	[$\mu\text{mol Cr/g Fe}$]	634.89	1.05	607.20 to 663.85
K_{ads}	[$\mu\text{mol/L}$]	4.41	1.02	4.30 to 4.51
k_{sorb}	[1/s]	4.12×10^{-5}	1.07	3.87×10^{-5} to 4.39×10^{-5}
k_{chem}	[g/ $\mu\text{mol/s}$]	1.86×10^{-6}	1.05	1.77×10^{-6} to 1.94×10^{-6}
f_{st}	[-]	10.18	1.02	9.97 to 10.39
f_q	[-]	3.16	1.00	3.159 to 3.161

concentration included an experiment at pH 7 under oxic conditions and one at pH 12 under anoxic conditions. These conditions were used to evaluate the influence on the removal efficiency of the magnetite coated sand due to increased oxygen levels, typical for surface waters and aquifers lacking electron donors, or due to an increased pH (pH 12) as it is common in chromite ore processing residues (COPR) (Geelhoed et al., 2002).

Under oxic conditions, the removal efficiency of the magnetite coated sand was hampered by the competing reaction of Fe(II) oxidation by O_2 , and was lower in comparison to anoxic conditions and 0.1 mM Cr (VI) with just 47.2% removal by the measurements and 41.4% within the model. In the presence of O_2 , Fe(II) sites react with both O_2 and Cr (VI), thus lowering the amount of accessible reactive Fe(II) for Cr(VI) reduction, yielding a subsequent decrease in the chromium removal potential from solution (Eary and Rai, 1988; Pettine et al., 1998). The measured oxygen concentrations throughout the experimental run time are listed in Table S1. At an alkaline pH, common for COPR environments (pH 10–12), only a small amount of chromium (~3% determined by the BTC) was removed by the magnetite coated sand. The issue of the decreased removal efficiency can be explained as passivation of the magnetite surface sites under alkaline conditions and is further addressed in the section on the surface microscopy analysis.

Two distinct sets of model parameters were necessary to fit the identical model formulation to either the 10% or the 100% case (see Table 3). The calculated maximum sorption capacity (q_{max}) for the 10% case of 1.37 $\mu\text{mol Cr/g sand}$ (350.43 $\mu\text{mol Cr/g Fe}$) was in good agreement with the batch experiment results reported in our previous paper (358 $\mu\text{mol Cr/g Fe}$) (Sorwat et al., 2020). For the 100% case, however, the fitted q_{max} with a value of 2.48 $\mu\text{mol Cr/g sand}$ (634.89 $\mu\text{mol Cr/g Fe}$) was approximately two times higher, comparable to the q_{max} of magnetite nanoparticles alone, as determined in a previous study (Sorwat et al., 2020). We speculate that this discrepancy may be due to the dislodgement of small, loosely attached magnetite particles from the surface of the sand grains as a result of abrasion during the column packing procedure. While this abrasion of micro-/nanoparticles would occur in both the 10% and 100% columns, their overall contribution to increased sorption is expected to be higher in the 100% case. The release of small magnetite particles due to abrasion would have led to their

settling at the column outlet, and their higher surface area would have acted to increase the maximum sorption capacity, as evidenced by the higher-than-expected fitted q_{max} .

Outflow measurements of Fe(tot) (Fig. S5) did not, however, show evidence of increased efflux of Fe from the 100% coated columns. Therefore, the microparticles likely remained trapped in the outflow filter (Fig. S6). An explanation for this discrepancy is further discussed in the section on chromium and iron extraction, focusing on the solid-state extractions of the sand before and after the reaction with Cr.

3.2. Adsorbent characterization

3.2.1. Chromium and iron extraction

Fig. 2 presents measured and simulated depth profiles of solid-bound Cr in all experimental setups after 22 h (the end of the experiment). As mentioned above, the lack of an extended tailing behavior in the Cr-BTCs provides strong evidence that Cr-removal is modulated by a combination of reversible and irreversible sorption, as parameterized herein. The inclusion of chemisorption (Eq. 5) in our reactive-transport model formulation adequately captured the depth profiles of Cr that remained attached to the magnetite coated sand. The oxidation of Fe(II) results in a loss of (reversible) sorption sites and thus a reduction in the maximum sorption capacity. The effect of the Fe(II)-Cr(VI) reaction on the maximum sorption capacity is plotted alongside the Cr depth profiles in Fig. 2b and e. Fig. 2c and f report the measured and simulated changes in Fe(II) over depth for the 100% and the 10% columns, respectively. In each case, the measured amount of Fe(II) was lower than expected based on the stoichiometry of the full oxidation reaction of Fe(II) coupled to Cr (VI) reduction, which requires 3 Fe(II):1 Cr(VI). The deviation from the expected stoichiometry suggests that alternative processes, in addition to pure oxidation resulted in an additional loss of Fe(II) unaccounted for by Cr(VI) reduction. This enhanced Fe(II) loss was likely driven by two main processes. First, the replacement/substitution of Fe(II) by Cr(III) in the magnetite structure can cause its release into the aqueous phase (Crean et al., 2012; Cutting et al., 2010; Telling et al., 2009). In the cited studies, the corresponding authors used X-ray magnetic circular dichroism (XMCD) spectroscopy to get a detailed insight into the reaction of Cr with Fe. The coincident results of these studies describe an additional loss of iron due to the incorporation of Cr(III) into the magnetite structure combined with a substitution of Fe, responsible for the deviation of the expected change in Fe(II) if the oxidation of Fe(II) would be the only reaction in the system. Specifically, Crean et al. (2012) measured a larger drop in Fe(II) site occupancy in magnetite octahedral spinel sites than expected based on the increase in Fe(III) site occupancy as a function of total Cr(VI) removal. In addition, as mentioned above, a loss of loosely bound iron due to abrasion of small particles in comparison to a loss of Fe(II) that would have remained trapped in the outflow filter (Fig. S6). To address this discrepancy in a systematic form, we chose to parameterize the stoichiometric coefficient for the Cr(VI) reduction (chemisorption) reaction (r_{chemi}) as a fitting parameter, f_{st} . For both the 10% and 100% model variants the calibrated value of f_{st} was close to 10, showing that in all experiments the Fe(II) loss (parameterized as oxidation, herein) was 3.33 times larger than expected. The coefficient, f_{st} , thus captures the lumped contributions of “pure oxidation” and additional losses of Fe(II), which are related to the oxidation reaction but do not lead to Fe(III) production, but rather a physical loss of Fe(II).

To address the issue of microparticle abrasion during the experimental runs, we performed additional tests using either the 10% or 100% magnetite per volume but with a lower total amount of material used in the columns injecting Milli-Q. Following the injection, we measured the amount of iron collected by the outflow filter and the amount of iron in the outflow after 5, 10, or 15 mL (a total of approximately 2.5 pore volumes) passing through the column. Via 1 M HCl extraction we verified a measurable loss of Fe (Table S2 and Fig. S6). An increased amount of total Fe (29.7 $\mu\text{M Fe}$, computed from total detected

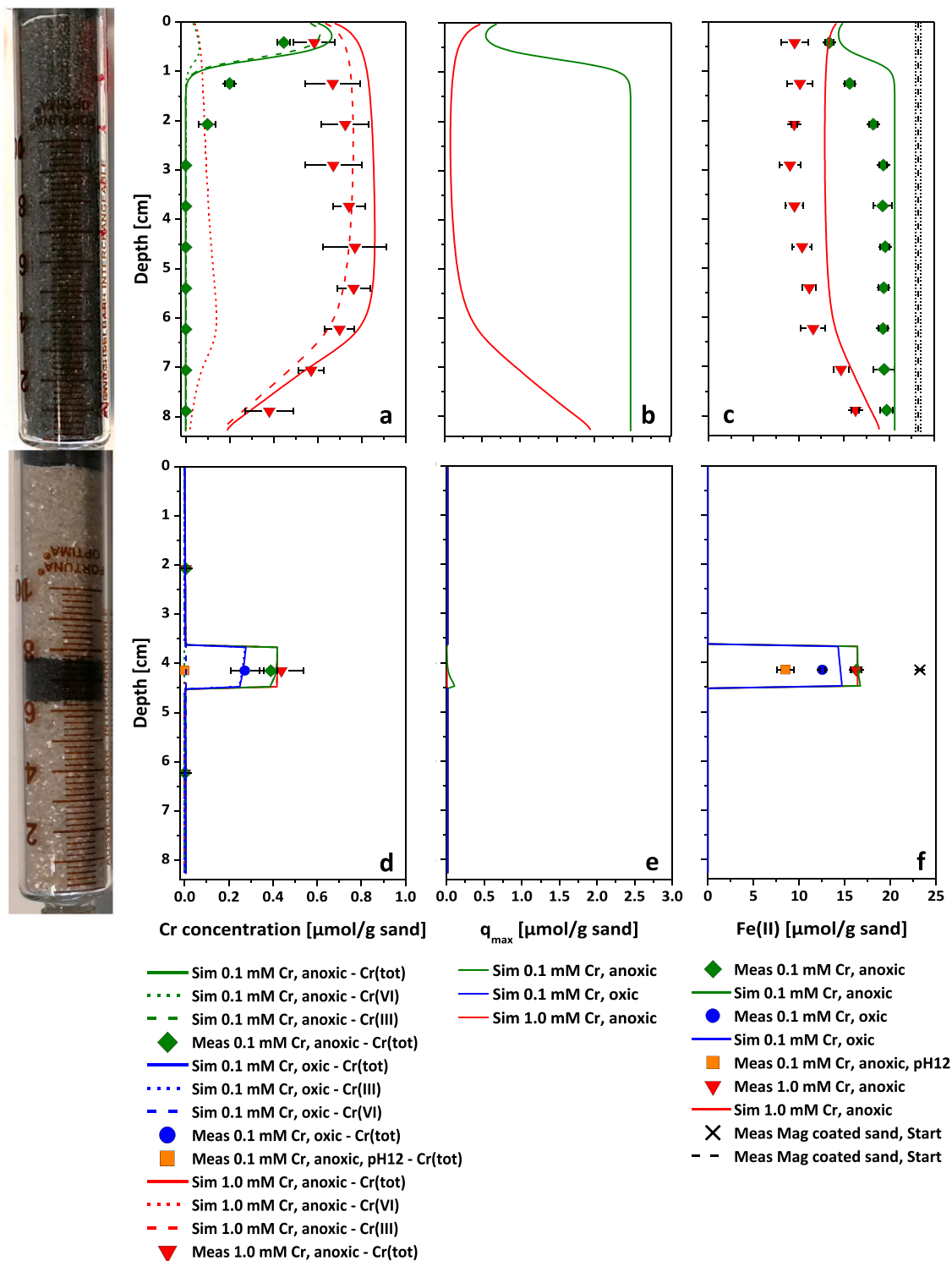


Fig. 2. Measured and simulated results for total chromium, maximum sorption capacity and iron II. (a+b+c) Results for the 100% columns. (d+e+f) Results for the 10% columns. The corresponding labels are displayed below the respective set of figures. Measured: Green diamonds: 0.1 mM Cr(VI) injection at pH 7 under anoxic conditions; Orange squares: 0.1 mM Cr(VI) injection at pH 12 under anoxic conditions; Red triangles: 1 mM Cr(VI) injection at pH 7 under anoxic conditions. The solid lines with the respective colors represent the simulated data. Dashed and dotted lines represent the simulated Cr(VI) and Cr(III) concentration, respectively (Note: These are shown for the 100%, 1 mM Cr(VI) case to illustrate the Cr-speciation at the end of the experiment). The black dashed line and black cross represent the Fe(II) concentration of the unreacted magnetite coated sand. (For interpretation of the references to colour in this figure legend, the reader is referred to the web version of this article.)

on the filter divided by the volume of solution passed through) was detected in the filter for the 100% column, in comparison to the 10% column ($0.2 \mu\text{M Fe}$), and on the order of that collected at the outflow (29.4 or $14.1 \mu\text{M Fe}$, respectively). The increased amount of iron trapped in the filter suggests that Fe could likely become detached from the coated sand and accumulate at the filter. The presence of a filter impeded the Fe (in particulate form) from flowing out, which is why no considerable increase in Fe breakthrough was detected in the effluent samples during our column experiments (Fig. S5), despite the evidence for iron loss from the extractions of the solid matrix.

3.3. Surface analysis

To elucidate the potential surface transformation of the magnetite coating after the reaction with Cr(VI) we imaged samples using scanning electron microscopy (SEM) at different magnifications. Fig. 3 provides results that focus on the comparison of the unreacted magnetite coated sand surface (Fig. 3a+b+c) with the magnetite coated sand grains treated with the highest Cr concentration (1.0 mM Cr) at pH 7 under anoxic conditions (Fig. 3d+e+f), and magnetite coated sand grains after the 0.1 mM Cr injection at pH 12, under anoxic conditions (Fig. 3g+h+i). The recorded images of the magnetite coated sand treated with 1.0 mM Cr at pH 7 under anoxic conditions (Fig. 3d+e+f) show no visible changes in surface morphology in comparison to the unreacted magnetite (Fig. 3a+b+c). Moreover, our results show that the surface of the coated sand, following the anoxic 0.1 mM Cr pH 12 injection, is dominated by large (μm -sized) plates (Fig. 3g+h+i), analogous to the morphology of synthetic goethite described by Kosmulski et al. (2004). Previous studies have also highlighted a similar shift in magnetite surface morphology at pH 12 (He and Traina, 2005, 2007), where a decreased removal efficiency under alkaline conditions can be

caused by a surface passivation due to the transformation of magnetite to goethite/maghemite. At a higher magnification (Fig. 3h+i), however, despite the change in morphology, magnetite particles were still visible on the surface, and sufficiently exposed to contribute to Cr(VI) reduction. In the anoxic 1.0 mM Cr , pH 7 treatment the magnetite surface was predominantly coated with magnetite nanoparticles (Fig. 3f) of seemingly identical size and shape as prior to the Cr injection (Fig. 3c), with no evidence of goethite plates along the grains. Thus, while the formation of goethite plates would have hampered the ability of the sand to reduce Cr(VI), we attribute the lack of Cr(VI) reduction in the pH 12 treatment to the pH-dependent surface charge of the exposed magnetite particles rather than the goethite plates. At neutral pH, the surface of magnetite is positively charged (PZC = 6.3–6.8) (Regazzoni et al., 1983). An increase to alkaline pH (pH 12) shifts the surface site speciation to a majority of negatively charged sites, yielding electrostatic repulsion between chromate oxyanions and the magnetite surface, thus inhibiting the sorption of Cr to the surface of magnetite and therefore the reduction of Cr(VI) by Fe(II) (He and Traina, 2005). (Note: No obvious changes in the surface morphology of magnetite are evident under oxic conditions at neutral pH (Fig. S7 c+d). Images for the uncoated pure sand are presented in the SI (Fig. S7 a+b)).

Energy-dispersive X-ray spectroscopy (EDX) confirmed the association of Cr with the surface of the magnetite coated sand grains. The recorded spectra for the 10% and the 100% columns are shown in Fig. S8 and Fig. S9, respectively. Additionally, Fig. S8 shows the spectra for unreacted magnetite coated sand and the 1 mM Cr(VI) treated uncoated sand. The determined weight percentages of Cr compared to other elements located on the surface of the grains for the different spectra are listed in Table S3. With these results we can confirm the trend for Cr sorption at different locations along the columns. We can see the same trend for the 100% columns with higher Cr content at the top parts for a

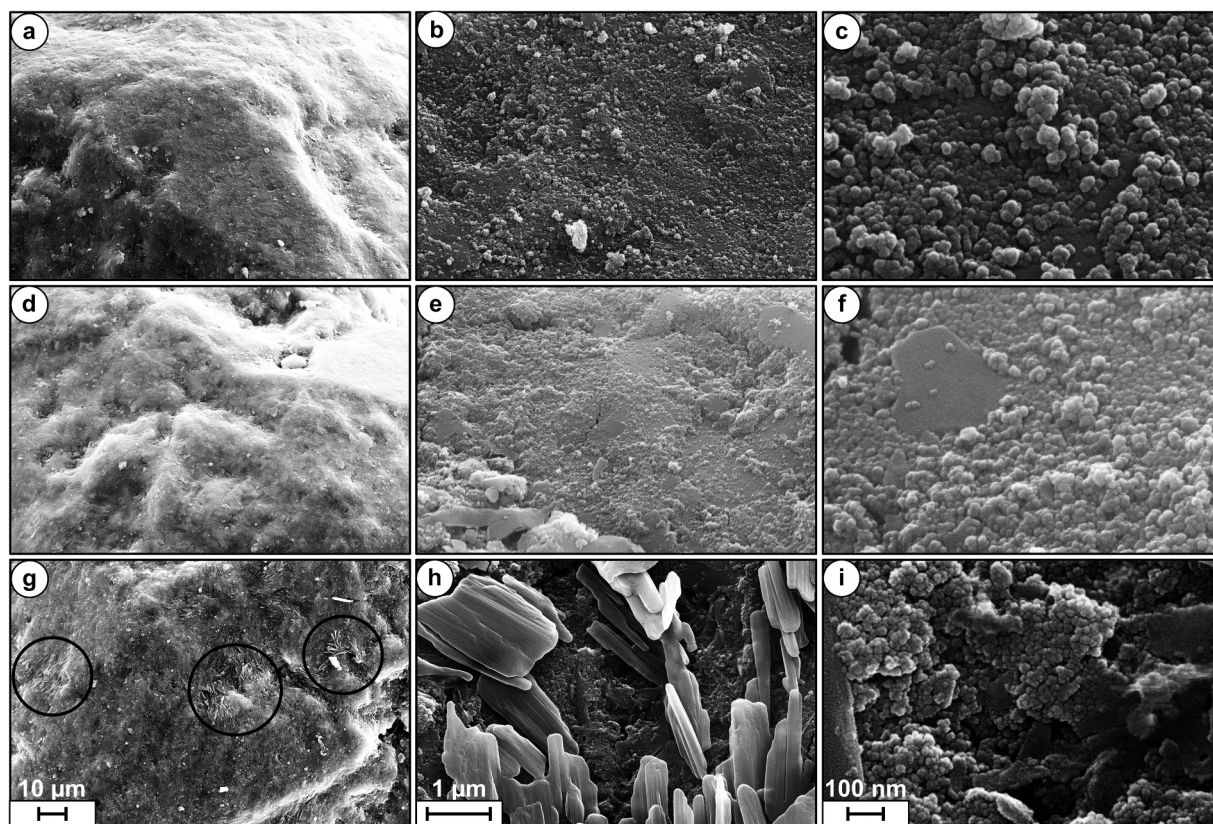


Fig. 3. Recorded SEM images of (a+b+c) the unreacted magnetite coated sand, (d+e+f) the 10% layer reacted with 1.0 mM Cr(VI) at pH 7 under anoxic conditions and (g+h+i) reacted with 0.1 mM Cr(VI) at pH 12 under anoxic conditions with a (a+d+g) 750x, (b+e+h) 18 kx and (c+f+i) 100 kx magnification. Black circles focus on areas with evidence of needles indicating transformation.

treatment with either 0.1 mM or 1.0 mM Cr compared to the solid extractions in Fig. 2a. Furthermore, we can confirm that more Cr is located at the magnetite grains in the top part of each 100% column in comparison to the 10% columns, although the same mass of Cr was injected.

4. Conclusions

In this study we combined experiments and process based modelling in order to quantify the efficiency of Cr(VI) removal from solution using magnetite-coated sand, a cheap and easy-to-handle material, which can be easily deployable in future water purification and remediation approaches. Specifically, our well-fitting model considers two-step sorption followed by the reduction of adsorbed Cr(VI) to Cr(III). This model formulation integrates recent developments in the conceptual understanding of the two-part magnetite-Cr reaction (Chang et al., 2021) and applies these in a system under flow-through conditions.

Our experiments and the corresponding model fit confirmed that a direct transfer of results obtained in batch systems to flow-through systems and up-scaling in porous media is challenging. In order to fit the measured data, the simulated maximum sorption capacity in the 10% columns confirmed the value determined in our previous batch study (Sorwat et al., 2020), whereas we needed a different set of parameters for the 100% columns. We attribute this to the loss of loosely attached coating particles which led to a release of small magnetite particles. Due to the inverse relationship between particle size and specific surface area (SSA) (Cornell and Schwertmann, 2003) the higher SSA likely led to an increased reactivity towards Cr(VI) and therefore to an increased maximum sorption capacity. We demonstrated the loss of smaller particles by quantifying iron trapped in the outflow filter following water saturation of the dry-packed sand matrix.

A relevant outcome of our study was that the stoichiometry of Cr removal and Fe oxidation differed from the expected 1:3 ratio. We speculate that this might be caused by the release of aqueous Fe(II) upon the replacement/substitution of Fe(II) by Cr(III) in the magnetite structure, or by the release of small Fe-bearing particles. As the Fe(II) demand observed in our study was three times higher than expected by stoichiometry, this discrepancy is significant for the design of remediation or water-treatment schemes involving magnetite-coated sands, and the observed phenomenon deserves further studies to elucidate the underlying mechanisms.

Our results show that magnetite coated onto sand is a promising remediation agent, able to remove and irreversibly sequester Cr(VI) from solution. Furthermore, the use of a surface coating rather than nanoparticles keeps the adsorbent in place and minimizes unwanted release of iron. The good agreement between our model formulation and measured data provides a useful tool to predict the reactivity and the removal efficiency of the magnetite coated sand that could be easily upscaled to large-scale remediation applications, such as permeable reactive barriers. In addition, we were able to show that the magnetite coating maintains a high removal capacity, albeit reduced by ~20%, even under oxic conditions. This is an important outcome as it shows that the material can still be used even when handled sub-optimally, as might be anticipated during actual field applications. A logical next step would be to increase the amount of material produced and test its performance in larger scale tank experiments and/or at Cr-contaminated sites. If the pH at these sites is very high, we cannot recommend using magnetite coated sands as remediation agent without the addition of acidifying agents to overcome the repulsion of chromate at the magnetite surface. Once the Cr is chemisorbed, such a pH control would no longer be necessary.

The novelty of our study is that it provides, via a combination of modelling and experimental data, a process based quantification of the efficiency of Cr(VI) removal from solution using a cheap, and easy to handle material which can be easily deployable in future water purification and remediation approaches.

CRedit authorship contribution statement

Julian Sorwat: Conceptualization, Methodology, Investigation, Writing, Visualization. **Adrian Mellage:** Conceptualization, Formal analysis, Investigation, Visualization. **Markus Maisch:** Investigation, Visualization. **Olaf A. Cirpka:** Conceptualization, Methodology, Writing. **Andreas Kappler:** Conceptualization, Supervision, Writing. **James M. Byrne:** Conceptualization, Supervision, Visualization, Writing, Project administration, Funding acquisition.

Declaration of Competing Interest

The authors declare that they have no known competing financial interests or personal relationships that could have appeared to influence the work reported in this paper.

Acknowledgements

This work was supported by funding awarded to J Byrne as part of the Baden Wuerttemberg RiSC program, and Deutsche Forschungsgemeinschaft DFG (BY 82/2-1). We also thank the DFG (INST 37/1027-1 FUGG) for financial support provided for the acquisition of the cryogenic focused ion beam scanning electron microscope. The authors gratefully acknowledge the Tübingen Structural Microscopy Core Facility (Funded by the Federal Ministry of Education and Research (BMBF) and the Baden-Württemberg Ministry of Science as part of the Excellence Strategy of the German Federal and State Governments) for their support & assistance in this work. Many thanks also to Sara Roci who contributed significantly to this work.

Appendix A. Supporting information

Supplementary data associated with this article can be found in the online version at [doi:10.1016/j.jhazmat.2021.125648](https://doi.org/10.1016/j.jhazmat.2021.125648).

References

- Avudainayagam, S., Megharaj, M., Owens, G., Kookana, R.S., Chittleborough, D., Naidu, R., 2003. Chemistry of chromium in soils with emphasis on tannery waste sites. *Rev. Environ. Contam. Toxicol.* 178, 53–91.
- Bailey, R.P., Bennett, T., Benjamin, M.M., 1992. Sorption onto and recovery of Cr(VI) using iron-oxide-coated sand. *Water Sci. Technol.* 26 (5–6), 1239–1244.
- Barnhart, J., 1997. Occurrences, uses, and properties of chromium. *Regul. Toxicol. Pharmacol.* 26, S3–S7 (0273-2300 (Print)).
- Bartlett, R., James, B., 1979. Behavior of chromium in soils: III. Oxidation. *J. Environ. Qual.* 8 (1), 31–35.
- Brezonik, P.L., Arnold, W.A., 2012. Water chemistry: fifty years of change and progress. *Environ. Sci. Technol.* 46 (11), 5650–5657.
- Buerge, I.J., Hug, S.J., 1999. Influence of mineral surfaces on chromium(VI) reduction by iron(II). *Environ. Sci. Technol.* 33 (23), 4285–4291.
- Chahbani, M.H., Tondeur, D., 2001. Pressure drop in fixed-bed adsorbers. *Chem. Eng. J.* 81, 23–34.
- Chang, J., Wang, H., Zhang, J., Xue, Q., Chen, H., 2021. New insight into adsorption and reduction of hexavalent chromium by magnetite: multi-step reaction mechanism and kinetic model developing. *Colloids Surf. A Physicochem. Eng. Asp.* 611, 125784.
- Coleman, T.F., Li, Y.Y., 1996. An interior trust region approach for nonlinear minimization subject to bounds. *Siam J. Optim.* 6 (2), 418–445.
- Cornell, R.M., Schwertmann, U., 2003. *The Iron Oxides: Structure, Properties, Reactions, Occurrences and Uses*. Wiley-VCH Verlag GmbH & Co. KGaA.
- Crean, D.E., Coker, V.S., van der Laan, G., Lloyd, J.R., 2012. Engineering biogenic magnetite for sustained Cr(VI) remediation in flow-through systems. *Environ. Sci. Technol.* 46 (6), 3352–3359.
- Cutting, R.S., Coker, V.S., Telling, N.D., Kimber, R.L., Pearce, C.I., Ellis, B.L., Lawson, R. S., van der Laan, G., Patrick, R.A.D., Vaughan, D.J., Arenholz, E., Lloyd, J.R., 2010. Optimizing Cr(VI) and Tc(VII) remediation through nanoscale biomineral engineering. *Environ. Sci. Technol.* 44, 2577–2584.
- Eary, L.E., Rai, D., 1988. Chromate removal from aqueous wastes by reduction with ferrous ion. *Environ. Sci. Technol.* 22 (8), 972–977.
- European Commission. Council Directive 98/83/EC of 3 November 1998 on the quality of water intended for human consumption. <http://eur-lex.europa.eu/legal-content/EN/TXT/?uri=CELEX%3A01998L0083-20151027>. Accessed 24 October 2020, 1998.
- Fantoni, D., Brozzo, G., Canepa, M., Cipolli, F., Marini, L., Ottonello, G., Zuccolini, M., 2002. Natural hexavalent chromium in groundwaters interacting with ophiolitic rocks. *Environ. Geol.* 42 (8), 871–882.

- Fendorf, S., Wielinga, B.W., Hansel, C.M., 2000. Chromium transformations in natural environments: the role of biological and abiological processes in chromium(VI) reduction. *Int. Geol. Rev.* 42 (8), 691–701.
- Fendorf, S.E., Li, G., 1996. Kinetics of chromate reduction by ferrous iron. *Environ. Sci. Technol.* 30 (5), 1614–1617.
- Geelhoed, J.S., Meeussen, J.C.L., Hillier, S., Lumsdon, D.G., Thomas, R.P., Farmer, J.G., Paterson, E., 2002. Identification and geochemical modeling of processes controlling leaching of Cr(VI) and other major elements from chromite ore processing residue. *Geochim. Cosmochim. Acta* 66 (22), 3927–3942.
- Harijan, D.K.L., Chandra, V., 2016. Environment friendly synthesis of magnetite–graphene composite for adsorption of toxic chromium (VI) ions from drinking water. *Environ. Progress Sustain. Energy* 35 (3), 700–705.
- He, Y.T., Traina, S.J., 2005. Cr(VI) reduction and immobilization by magnetite under alkaline pH conditions: the role of passivation. *Environ. Sci. Technol.* 39 (12), 4499–4504.
- He, Y.T., Traina, S.J., 2007. Transformation of magnetite to goethite under alkaline pH conditions. *Clay Miner.* 42 (1), 13–19.
- Jin, W., Du, H., Zheng, S., Zhang, Y., 2016. Electrochemical processes for the environmental remediation of toxic Cr(VI): a review. *Electrochim. Acta* 191, 1044–1055.
- Jung, Y., Choi, J., Lee, W., 2007. Spectroscopic investigation of magnetite surface for the reduction of hexavalent chromium. *Chemosphere* 68 (10), 1968–1975.
- Kango, S., Kumar, R., 2016. Magnetite nanoparticles coated sand for arsenic removal from drinking water. *Environ. Earth Sci.* 75 (5), 381.
- Kaprara, E., Kazakis, N., Simeonidis, K., Coles, S., Zouboulis, A.I., Samaras, P., Mitrakas, M., 2015. Occurrence of Cr(VI) in drinking water of Greece and relation to the geological background. *J. Hazard. Mater.* 281, 2–11.
- Kosmulski, M., Durand-Vidal, S., Mączka, E., Rosenholm, J.B., 2004. Morphology of synthetic goethite particles. *J. Colloid Interface Sci.* 271 (2), 261–269.
- Meranger, J.C., Subramanian, K.S., Chalifoux, C., 1979. A national survey for cadmium, chromium, copper, lead, zinc, calcium, and magnesium in Canadian drinking water supplies. *Environ. Sci. Technol.* 13 (6), 707–711.
- Mikutta, C., Wiederhold, J.G., Cirpka, O.A., Hofstetter, T.B., Bourdon, B., Gunten, U.V., 2009. Iron isotope fractionation and atom exchange during sorption of ferrous iron to mineral surfaces. *Geochim. Cosmochim. Acta* 73 (7), 1795–1812.
- Owlad, M., Aroua, M.K., Daud, W.A.W., Baroutian, S., 2009. Removal of hexavalent chromium-contaminated water and wastewater: a review. *Water Air Soil Pollut.* 200 (1), 59–77.
- Petosa, A.R., Jaisi, D.P., Quevedo, I.R., Elimelech, M., Tufenkji, N., 2010. Aggregation and deposition of engineered nanomaterials in aquatic environments: role of physicochemical interactions. *Environ. Sci. Technol.* 44 (17), 6532–6549.
- Pettine, M., D'Ottone, L., Campanella, L., Millero, F.J., Passino, R., 1998. The reduction of chromium (VI) by iron (II) in aqueous solutions. *Geochim. Cosmochim. Acta* 62 (9), 1509–1519.
- Phenrat, T., Kim, H.J., Fagerlund, F., Illangasekare, T., Tilton, R.D., Lowry, G.V., 2009. Particle size distribution, concentration, and magnetic attraction affect transport of polymer-modified Fe₀ nanoparticles in sand columns. *Environ. Sci. Technol.* 43 (13), 5079–5085.
- Phenrat, T., Cihan, A., Kim, H.J., Mital, M., Illangasekare, T., Lowry, G.V., 2010. Transport and deposition of polymer-modified Fe₀ nanoparticles in 2-D heterogeneous porous media: effects of particle concentration, Fe₀ content, and coatings. *Environ. Sci. Technol.* 44 (23), 9086–9093.
- Regazzoni, A.E., Blesa, M.A., Maroto, A.J.G., 1983. Interfacial properties of zirconium dioxide and magnetite in water. *J. Colloid Interface Sci.* 91 (2), 560–570.
- Ren, G., Wang, X., Huang, P., Zhong, B., Zhang, Z., Yang, L., Yang, X., 2017. Chromium (VI) adsorption from wastewater using porous magnetite nanoparticles prepared from titanium residue by a novel solid-phase reduction method. *Sci. Total Environ.* 607–608, 900–910.
- Richard, F.C., Bourg, A.C.M., 1991. Aqueous geochemistry of chromium: a review. *Water Res.* 25 (7), 807–816.
- Robles-Camacho, J., Armienta, M.A., 2000. Natural chromium contamination of groundwater at León Valley, México. *J. Geochem. Explor.* 68 (3), 167–181.
- Royal, S. and Royal, E., 2004. *Academy of Nanoscience and Nanotechnologies: Opportunities and Uncertainties*. RS policy document, Royal Society.
- Saputro, S., Yoshimura, K., Matsuoka, S., Takehara, K., Narsito, Aizawa, J., Tennichi, Y., 2014. Speciation of dissolved chromium and the mechanisms controlling its concentration in natural water. *Chem. Geol.* 364, 33–41.
- Shampine, L.F., 1997. The MATLAB ODE suite. *SIAM J. Scientific Comput.* 18, 1–22.
- Sharma, S.K., Petruskevski, B., Amy, G., 2008. Chromium removal from water: a review. *J. Water Supply Res. Technol. Aqua* 57 (8), 541–553.
- Singh, D.B., et al., 1993. The use of hematite for chromium(VI) removal. *J. Environ. Sci. Health Part A Environ. Sci. Eng. Toxicol.* 28 (8), 1813–1826.
- Sorwat, J., Mellage, A., Kappler, A., Byrne, J.M., 2020. Immobilizing magnetite onto quartz sand for chromium remediation. *J. Hazard. Mater.* 400, 123139.
- Sperlich, A., Werner, A., Genz, A., Amy, G., Worch, E., Jekel, M., 2005. Breakthrough behavior of granular ferric hydroxide (GFH) fixed-bed adsorption filters: modeling and experimental approaches. *Water Res.* 39 (6), 1190–1198.
- Stookey, L.L., 1970. Ferrozine—a new spectrophotometric reagent for iron. *Anal. Chem.* 42 (7), 779–781.
- Sundman, A., Vitzthum, A.L., Adaktylos-Surber, K., Figueroa, A.I., van der Laan, G., Daus, B., Kappler, A., Byrne, J.M., 2020. Effect of Fe-metabolizing bacteria and humic substances on magnetite nanoparticle reactivity towards arsenic and chromium. *J. Hazard. Mater.* 384, 121450.
- Telling, N.D., Coker, V.S., Cutting, R.S., van der Laan, G., Pearce, C.I., Patrick, R.A.D., Arenholz, E., Lloyd, J.R., 2009. Remediation of Cr(VI) by biogenic magnetic nanoparticles: an x-ray magnetic circular dichroism study. *Appl. Phys. Lett.* 95, 163701.
- Tratnyek, P.G., Johnson, R.L., 2006. Nanotechnologies for environmental cleanup. *Nano Today* 1 (2), 44–48.
- US Environmental Protection Agency, National primary drinking water regulations, 2009. <https://www.epa.gov/ground-water-and-drinking-water/national-primary-drinking-water-regulations>. Accessed 21 October 2020.
- US Environmental Protection Agency, Office of Drinking Water, Health Advisory—Chromium. Washington, DC, 1987.
- Verbrinnen, B., Block, C., Lievens, P., Van Brecht, A., Vandecasteele, C., 2013. Simultaneous removal of molybdenum, antimony and selenium oxyanions from wastewater by adsorption on supported magnetite. *Waste Biomass Valoriz.* 4, 635–645.
- Wang, T.-H., Li, M.-H., Teng, S.-P., 2009. Bridging the gap between batch and column experiments: a case study of Cs adsorption on granite. *J. Hazard. Mater.* 161 (1), 409–415.
- World Health Organization, Guidelines for Drinking-water Quality. Health Criteria and Other Supporting Information, 1996, 2.
- Xu, Y., Zhao, D., 2007. Reductive immobilization of chromate in water and soil using stabilized iron nanoparticles. *Water Res.* 41 (10), 2101–2108.
- Zach-Maor, A., Semiat, R., Shemer, H., 2011. Synthesis, performance, and modeling of immobilized nano-sized magnetite layer for phosphate removal. *J. Colloid Interface Sci.* 357 (2), 440–446.
- Zach-Maor, A., Semiat, R., Shemer, H., 2011. Fixed bed phosphate adsorption by immobilized nano-magnetite matrix: experimental and a new modeling approach. *Adsorption* 17 (6), 929–936.